Sequential Electrochemical Unzipping of Single-Walled Carbon Nanotubes to Graphene Ribbons Revealed by *in Situ* Raman Spectroscopy and Imaging

Robin John,[†,▽] Dhanraj B. Shinde,[‡,▽] Lili Liu,[§] Feng Ding,[§,⊥] Zhiping Xu,[∥] Cherianath Vijayan,[†] Vijayamohanan K. Pillai,[#,*] and Thalappil Pradeep[△,*]

[†]Department of Physics, Indian Institute of Technology Madras, Chennai 600 036, India, [‡]Physical and Materials Chemistry Division, National Chemical Laboratory, Pune 411 008, India, [§]Beijing Computational Science Research Center, Beijing 100084, People's Republic of China, [⊥]Institute of Textiles and Clothing, Hong Kong Polytechnic University, Kowloon, Hong Kong S. A. R., People's Republic of China, [∥]Department of Engineering Mechanics, Tsinghua University, Beijing 100084, People's Republic of China, [#]Central Electrochemical Research Institute, Karaikudi 630 006, India, and [△]DST Unit of Nanoscience and Thematic Unit of Excellence, Department of Chemistry, Indian Institute of Technology Madras, Chennai 600 036, India. [▽]R. John and D. B. Shinde contributed equally.

ABSTRACT We report an *in situ* Raman spectroscopic and microscopic investigation of the electrochemical unzipping of single-walled carbon nanotubes (SWNTs). Observations of the radial breathing modes (RBMs) using Raman spectral mapping reveal that metallic SWNTs are opened up rapidly followed by gradual unzipping of semiconducting SWNTs. Consideration of the resonant Raman scattering theory suggests that two metallic SWNTs with chiralities (10, 4) and (12, 0) get unzipped first at a lower electrode potential (0.36 V) followed by the gradual unzipping of another two metallic tubes, (9, 3) and (10, 1), at a relatively higher potential (1.16 V). The semiconducting SWNTs with chiralities (11, 7) and (12, 5), however, get open up gradually at ±1.66 V. A rapid decrease followed by a subsequent gradual decrease in the metallicity of the SWNT ensemble as revealed from a remarkable variation of the peak width of the G band complies well with the variations of RBM. Cyclic voltammetry also gives direct evidence for unzipping in terms of improved capacitance after oxidation followed by more important removal of oxygen functionalities during the reduction step, as reflected in subtle changes of the morphology confirming the formation of graphene nanoribbons. The density functional-based tight binding calculations show additional dependence of chirality and diameter of nanotubes on the epoxide binding energies, which is in agreement with the Raman spectroscopic results and suggests a possible mechanism of unzipping determined by combined effects of the structural characteristics of SWNTs and applied field.

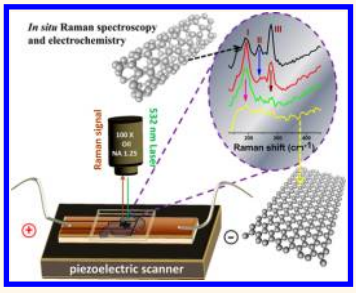

KEYWORDS: graphene · single-walled carbon nanotubes · electrochemistry · Raman spectral mapping · density functional-based tight binding calculations

Carbon has been exciting to scientists for centuries and still continues to fascinate the scientific community in the form of nanometer-sized allotropes such as bucky balls[1] and nanotubes[2] and, more recently, in the form of the ideal atomic layer, graphene.[3] Numerous chemical variants of these have also been explored. Both single-walled carbon nanotubes (SWNTs) and graphene possess unique properties with diverse applications in electronics[4−6] and quantum computing[7] and, above all, possess the ability to unravel many fundamental questions related to ballistic-thermal and -electronic transport.[8−13] SWNTs require high purity and accurate characterization in terms of chiralities and length and diameter distribution for them to be used in most of the specific applications. A similar scenario exists in the case of graphene as well, being vulnerable to drastic changes in the band structure with increasing number of layers,[14] changes in the edge states,[15] *etc.*

It has been understood both theoretically and experimentally that graphene ribbons can have a band gap that could be tuned by varying its width[16,17] and geometry.[18] Nanoribbons are considered important because of the emerging local magnetism with very specific edge states.[19] There are also attempts to use these nanoibbons in electronics by visualizing them as active channel

* Address correspondence to pradeep@iitm.ac.in; vijay@cecri.res.in.

Received for review June 28, 2013 and accepted December 5, 2013.

Published online December 05, 2013
10.1021/nn403289g

materials in field effect transistors.[20,21] Hence, it is desirable to have a precise method without any over-oxidation to convert specific SWNTs to graphene nanoribbons and thereby create graphenic materials of desired properties. This concept was also aided by the ability to separate SWNTs according to their metallicity[22] and diameter,[23] which eventually helps in getting graphene ribbons of specific width and edge structure. In this context, recently, Dhanraj *et al.* devised an electrochemical route to convert multiwalled nanotubes into multilayered graphene nanoribbons (GNRs).[24] In brief, nanoribbons of a few layers of graphene have been prepared from carbon nanotubes (CNT) by a two-step electrochemical approach consisting of oxidation of CNTs at controlled potential, followed by reduction to form GNRs having smooth edges and fewer defects, as evidenced by multiple characterization techniques, including Raman spectroscopy, atomic force microscopy, and transmission electron microscopy (TEM). However, neither the role of electric field nor the mechanism of opening and the sequence of events between CNT breaking (oxidative cleavage of the C−C bond) and GNR formation has been probed. Answers to questions such as, is the unzipping fundamentally different for metallic and semiconducting CNTs, where does the curvature break, and what is the reason for selecting a mixture of semiconducting and metallic CNTs, have not been explored, although both single and multiwalled CNTs have been shown to generate GNRs with controlled widths and fewer defects. An *in situ* spectroscopic investigation of various stages of the above sequential processes can possibly reveal the mechanism of unzipping of nanotubes and selective breaking, if any. This will also be important to understand the mechanism of unzipping of SWNTs to GNRs by other methods such as laser cutting and chemical unzipping.[25,26]

RESULTS AND DISCUSSION

We report an *in situ* Raman spectroscopic and microscopic investigation (see Methods and Materials for a detailed description) of the electrochemical unzipping of SWNTs to form graphene ribbons. It was desirable to have a different electrochemical setup that enables this process to be observable in real time. An electrochemical cell was constructed by making a discontinuity on a conducting indium tin oxide (ITO)-coated glass plate to have both electrodes (working and counter) laterally mounted on the same surface in order to suit Raman measurements. The constraint due to the microscopic setup (limited working distance of the objective used) did not allow us to have a cell thicker than 0.24 mm. SWNT dispersion (Methods and Materials) in *N*,*N*-dimethyl formamide (DMF) was deposited on the working electrode, which was kept under the microscope. A particular portion of the

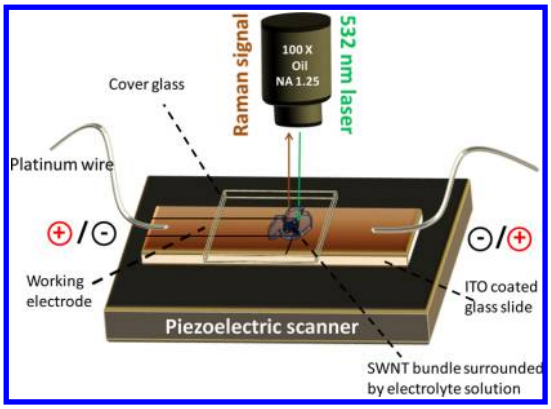

Figure 1. Schematic of the experimental setup used for the *in situ* Raman spectroscopic investigation of the unzipping of SWNTs with orthogonal laser illumination and spectral collection in the backscattering geometry, inside the electrochemical cell. Various parts of the electrochemical cell and essential parts of the Raman spectrometer are labeled. The connections to the electrodes from the dc source are given using a 0.1 mm thick Pt wire.

nanotube sample, say a bundle which contains many SWNTs, was selected and continually imaged using Raman spectral features keeping the same region (20 μm × 20 μm) by varying the potentiostatic conditions. A schematic of the experimental setup used for the study is given in Figure 1 (details are given in the Materials and Methods).

An average micro-Raman spectrum from the drop-casted SWNT on the working electrode shows all the expected features such as the radial breathing modes (RBMs) appearing in the spectral window of 180−280 cm^{-1}, a not so prominent D band (1345 cm^{-1}), a G band (1593 cm^{-1}), and a 2D band (2660 cm^{-1}). A high-resolution RBM spectrum collected for the same sample using a grating of 1800 grooves/mm shows three distinct features at 196 (designated here on as RBM I), 240 (RBM II), and 276 (RBM III) cm^{-1}. RBMs II and III indicate the presence of a number of metallic nanotubes (mSWNT), and RBM I is due to a couple of semiconducting tubes (sSWNT) with different chiralities. By considering the resonance (532 nm laser, 2.33 eV) condition of our measurement, the bundling of SWNTs, the peak positions, and the peak width of ω_{RBM}, a more reasonable assignment of the chiralities can be suggested as follows: 196 cm^{-1} [(11, 7) or (12, 5), interband transition E_{33} = 2.37 or 2.35 eV, diameter d = 1.25 or 1.2 nm, semiconducting], 240 cm^{-1} [(10, 4) or (12, 0), E_{11} = 2.24 or 2.23 eV, d = 0.98 or 0.94 nm, metallic], 276 cm^{-1} [(9, 3) or (10, 1), E_{11} = 2.43 or 2.41 eV, d = 0.85 or 0.83 nm, metallic].[27−29] While the data from one set of SWNT bundles is presented here, data from other bundles are presented in the Supporting Information. Each data set has also been checked for reproducibility.

Spatially resolved Raman spectra (see Materials and Methods) were collected in the spectral window of 0−3900 cm^{-1} for various electrochemical conditions

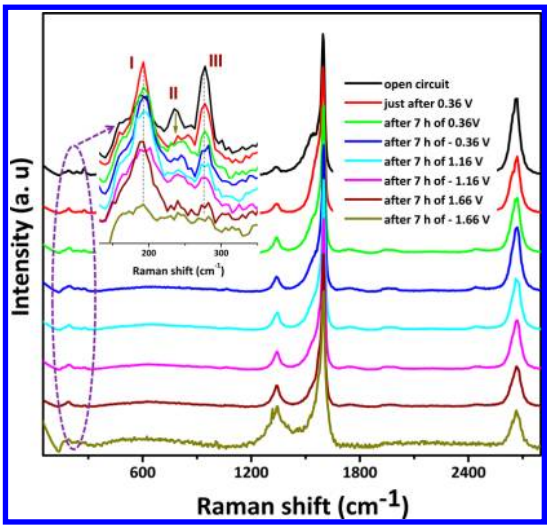

Figure 2. Raman spectra of gradual unzipping of SWNTs. Inset displays the averaged RBM spectra from the sample for various conditions. The black trace is that of the parent material. The red trace (immediately after the application of 0.36 V) shows near-complete disappearance of the second RBM. The third RBM disappears with various conditions, as one can see from the decrease in intensity of the peak around 276 cm^{-1}. Various conditions are labeled by different color. A considerable decrease in the width of the G band is observed, suggesting the reduction in metallicity along with an increase in the D band, which implies increased defects formed during unzipping. The variations in the 2D band at 2660 cm^{-1} band have been discussed elsewhere in the text. Featureless regions of the spectra are used to place the insets.

(labeled in Figure 2). Figure 2 shows the evolution of the average spectral features of the SWNT sample upon various cycles of electrochemical processes. A decrease in peak width of the G band was observed as time evolves and with increased potentials, which is indicative of reduction in the metallicity of the SWNT bundle. There was also an increase in the D band intensity, suggesting increased defects (see Figures 4 and 5 and the subsequent text for detailed discussion). The spectral position of the 2D band remains unchanged with a slight decrease in the peak width, suggesting the single-layer nature of the formed graphene ribbon with uncoupled ribbons. The inset of Figure 2 gives the evolution of the three RBMs of the average spectrum collected from the SWNT bundle, say RBM I (196 cm^{-1}), RBM II (240 cm^{-1}), and RBM III (276 cm^{-1}), which are labeled in the graph as I, II, and III, respectively. It is evident that immediately after the application of 0.36 V (red trace) to the working electrode, the intensity of feature II, corresponding to SWNTs with chiralities (10,4) and (12, 0), gradually disappears along with a considerable decrease in the intensity of feature III.

This remarkable change in RBM II *suggests rapid unzipping at a relatively lower anodic potential.* The subsequent steps show a gradual decrease in the intensity of RBM III, although the intensity of feature I was almost constant. However, after 7 h of application of 1.66 V to the working electrode, the intensity of RBM III (mSWNT) almost disappears (wine red colored trace), while the intensity of RBM I (another type of sSWNT) disappears only after the application of −1.66 V. The electrochemical potentials have been calibrated by carrying out separate experiments under identical conditions of the two-electrode *in situ* electrochemical cells in a three-electrode setup using a mercury/mercurous sulfate reference electrode. The hump still existing at the position of RBM II at the higher potentials is due to the fact that the spectra given in Figure 2 are averages of all the spectra collected throughout the region of the SWNT bundle. Upon examination of smaller areas, we see that there is a complete disappearance of this band immediately after the application of 0.36 V (Figure S1). We believe that there are inhomogeneities in the potential across a large area, and unzipping proceeds only slowly in such regions, explaining this overall spectral behavior.

Images corresponding to different phonon modes in SWNTs were filtered from the spectral map, and they reveal similar morphology, confirming the presence of high-quality SWNTs. A comparison of the images obtained from specific vibrational features for various electrochemical oxidizing conditions further confirms the sequential unzipping of different kinds of SWNTs to form graphene ribbons. Figure 3 compares the morphological features filtered using RBM I (178−206 cm^{-1}), RBM II (228−256 cm^{-1}), and RBM III (264−288 cm^{-1}) for potentials of 0 V (open circuit with no external bias), 0. 36 V (immediately after the application), and 1.16 and 1.66 V, applied to the working electrode for 7 h each. Three columns contain images filtered using RBM features of three pairs of SWNTs. The first column (RBM I) is the image due to sSWNTs (11, 7) or (12, 5), and the second (RBM II) and third (RBM III) columns correspond to mSWNTs (10, 4) or (12, 0) and (9, 3) or (10, 1), respectively. The spectral window for each set of RBMs is given at the top of each column. Each row corresponds to various potentiostatic conditions (as labeled at the left of each column) showing a different extent of oxidation of various types of nanotubes. The corresponding images after intermittent reducing potentials (by the application of −0.36, −1.16, and −1.66 V for 7 h) are shown in Figure S2 (Supporting Information).

The first row (Figure 3a−c) shows the presence of the three RBMs prior to the application of potential (*i.e.*, open circuit with no external bias denoted by 0 V) to the electrodes of the cell. The second row shows the presence of RBM I (d) and RBM III (f) in the imaged structure with a disappearance of the image filtered using RBM II (e) immediately after the application of 0.36 V to the working electrode. This is indicative of the rapid unzipping of two of the mSWNTs, (10, 4) and (12, 0). Figure 3 h and i show the absence of RBMs II

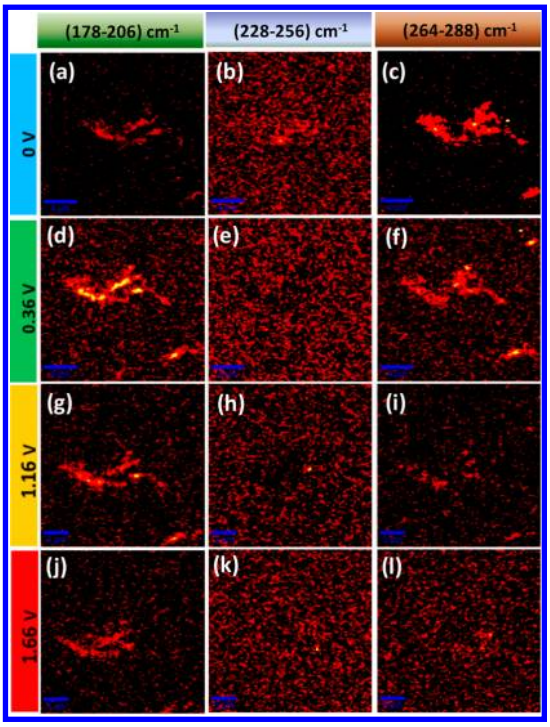

Figure 3. Evolution of the RBM region during electrochemical unzipping. Three columns contain images filtered using the RBMs of three different types of SWNTs. RBM I is due to sSWNTs (filtering windows is 178−206 cm^{-1}), whereas RBMs II and III are from mSWNTs (228−256 and 264−288 cm^{-1}, respectively). Each row corresponds to various stages of unzipping (corresponding to different oxidizing potentials as labeled at the left of each column) for the disappearance of various types of nanotubes. Raman images a−c show the presence of the three types of SWNTs prior to the application of potential (open circuit, *i.e.*, zero applied bias) to the electrodes of the cell. The second row shows the presence of RBM I (d) and RBM III (f) in the imaged structure with a disappearance of the image due to RBM II (e) immediately after the application of 0.36 V to the working electrode; images h and i show the absence of RBM II and III (mSWNTs), respectively, after the application of 1.16 V for a period of 7 h to the working electrode. Image j shows clear reduction in the intensity of RBM I throughout the bundle, along with the absence of RBM II (k) and III (l) after the application of 1.66 V to the working electrode for a period of 7 h. The color scaling varies slightly in each of the figures as the absolute intensities may not be the same in all the images. While the scale bar is 4 μm for images in the first two rows (a−f), it is 3 μm for the last two rows (g−l).

and III, suggesting the unzipping of another two types of mSWNTs, (9, 3) and (10, 1), after the application of 1.16 V for a period of 7 h. Figure S1 (Supporting Information) shows the disappearance of RBM I, suggesting the opening of sSWNTs (11, 7) and (12, 5) with the disappearance of the 196 cm^{-1} peak after the application of −1.66 V for a period of 7 h.

Although specific morphological features due to the three RBMs disappear sequentially with the application of the electric field, other morphological features filtered using D, G, and 2D remain more or less invariant. This is especially significant for unraveling the sequence of events associated with defect generation and lose of curvature. Figure 4 shows the Raman images filtered from 1320 to 1380 cm^{-1} (D band), 1565−1615 cm^{-1} (G), and 2620−2700 cm^{-1} (2D) before (a, b, and c) and after (d, e, and f) electrochemical processing. It is self-evident that the image filtered from G and 2D remains intact, whereas the features due to the D band are enhanced during the process, indicating additional defects formed upon unzipping (shown in Figure 4d). These preserved features arising from the planar sp^2-hybridized hexagonal carbon lattice along with the disappearance of RBMs suggest the unzipping of SWNTs to form GNRs. The images filtered using D, G, and 2D bands for the intermediate steps (immediately after the application of 0.36, 0.36, −0.36, 1.16, −1.16, and 1.66 V applied continuously for 7 h) are shown in Figures S3, S4, and S5. Additional measurements have been conducted on different bundles to confirm this phenomenon (Figures S6, S7, and S8). Formation of graphene ribbons was confirmed by TEM (Figures S9 and 10).

The relative intensity of RBM III with respect to that of RBM I (blue scatter) plotted in Figure 5a clearly shows a reduction at various steps (electrochemical conditions), numbered from 1 to 7 (same order as in Figure 2). We have excluded the eighth step (*i.e.*, −1.66 V applied to the working electrode) as in most cases the RBMs I and III are not present or are negligible to take a ratio. A considerable increase in the intensity of the D (1345 cm^{-1}) band is observed with each step. The I_D/I_G ratio has increased (Figure 2) from 0.039 (for open circuit) to 0.246 (after the application of −1.66 V for 7 h), suggesting the unzipping of SWNTs along with the addition of some undesirable defects. We have tried to analyze the G band and a broad shoulder present at its lower wavenumber region by deconvoluting the region from 1520 to 1610 cm^{-1} with two adjacent Lorentzian peaks (see a representative fit in Figure S11). The peak in the spectral range of 1520 to 1580 cm^{-1} (labeled as G* here on) accounts for the metallicity of the bundle, whose position and width vary with the electrochemical conditions. The peak width of the G (1596 cm^{-1}) band decreased from 23 cm^{-1} for the pristine SWNT to 18 cm^{-1} for the seventh step with a small increase to 19 cm^{-1} for the last step, *i.e.*, application of −1.66 V for 7 h. This variation in the peak width of the G band is also displayed in Figure 5a (wine color scatter), against various steps. The data plotted are the average of the information from four sets of *in situ* Raman spectroscopic data. The standard deviation is given as the error bar. The G* band shows a large decrease in its area and width along with a shift of the center maximum of the Lorentzian peak (details are given in Table S1 and Figure S12). This along with the variation in the RBM intensity ratio (blue scatter) explicitly confirms reduction

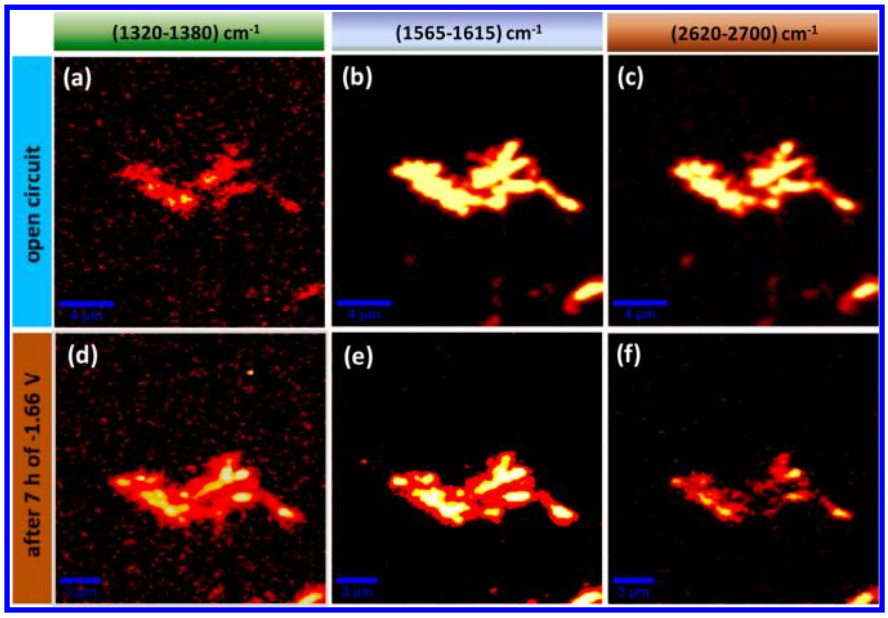

Figure 4. Transformation of SWNTs to graphene ribbons. The first row (a, b, and c) presents the images of the SWNT prior to the electrochemical unzipping, filtered using D (1320−1380 cm^{-1}), G (1565−1615 cm^{-1}), and 2D (2620−2700 cm^{-1}) bands, respectively (scale bar is 4 μm). The second row (e, f, and g) shows the images of the unzipped SWNTs filtered using D, G, and 2D bands. The presence of the G and 2D bands suggests that the sp^2-hybridized carbon structure is intact with an increase in the defect density (scale bar is 3 μm).

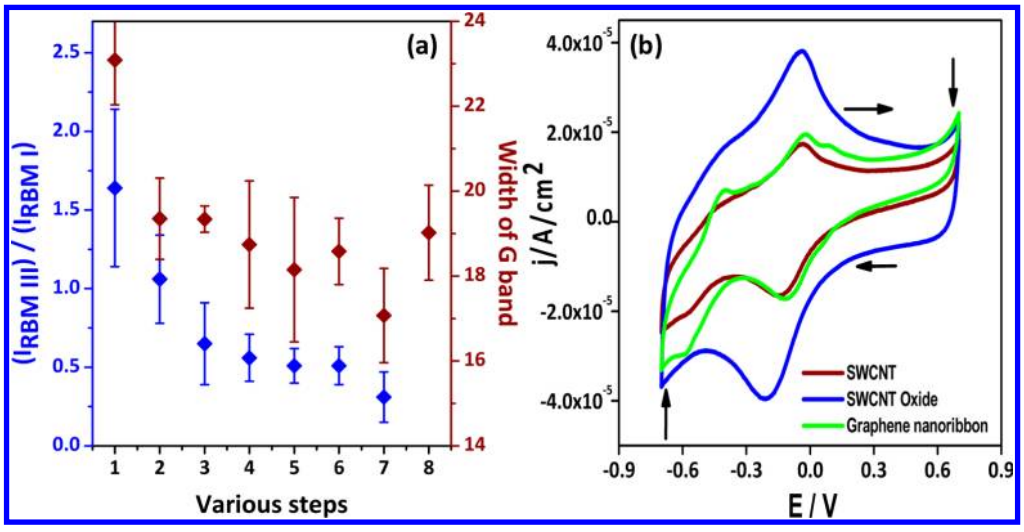

Figure 5. (a) Variation in the intensity ratios of the third RBM to that of the first RBM (blue) and variation of the peak width of the G band (wine color) for various steps (electrochemical conditions labeled in Figure 2 in the same order). Each point is the mean of the ratios from all four sets of *in situ* Raman data considered in the article. Their standard deviation is given as the error bar. (b) Cyclic voltammograms of pristine SWNT mixture, SWNT oxide, and graphene nanoribbons in the potential window from −0.7 to 0.7 V *vs* MMS in 0.5 M H_2SO_4 (same as used for the *in situ* Raman measurements) using a glassy carbon electrode at 100 mV/s scan rate. Arrows in the figure indicate the potential where SWNTs are selectively oxidized or reduced.

in metallicity.[30] We have also fitted the 2D band with a Lorentzian to measure the variation accurately. It is seen that there is a decrease in the intensity of the 2D band as the transformation progresses. We have also found from the spectral deconvolution data that there is a decrease in the width of the 2D band (Figure S13), which is an indication of the decoupling of the layers: the separation of individual tubes from one another upon unzipping in this particular experiment. As the sample under study was a bundle (not isolated SWNTs), it is intuitive that the integrity of the bundle might be affected by the unzipping process, as evident from Figure S10. However, it is difficult to know the details of the modification happening to the bundle using the available observations. The variation of the RBM at negative electrode potentials can happen only after the prior application of a positive potential. This suggests that the oxidation followed by reduction enhances unzipping.

The applied electric field initiates the breaking of sp^2 carbon bonds, perhaps at the middle (longitudinal) region of the side wall of the nanotubes, where a few topological defects can act as the epicenter (Stone–Wales defects). The above argument is supported by molecular dynamic simulations on MWNTs[31] and our TEM measurements (Figure S10 D). This defect generation continues in the longitudinal direction due to the field gradient, as evidenced by the subtle changes in the voltammogram (Figure 5b) similar to the changes seen in *in situ* Raman features. Broken SWNTs along a straight line are stretched farther away by the tension in the curved surface, which could result in the transformation into graphene oxide layers.[32] Cyclic voltammograms for the oxidation of SWNTs within the potential window from −0.7 to 0.7 V (*vs* mercury/mercurous sulfate (MMS) reference electrode) show surface-confined peaks at the beginning with a capacitance value of 50 F/g. However, after 7 h of oxidation at a potential of 0.7 V, there is a large increase in the capacitance (83 F/g), partly due to the change in surface area originating from the morphological changes and the remaining contribution due to the creation of oxygen-containing moieties.

More significantly, the increase in nonfaradaic current with time suggests subtle morphological changes, including that of the area. By keeping the potential at 0.7 V for 7 h, the oxidation of SWNTs generates an enormous number of oxygen functionalities (mainly for semiconducting types). At the end, interestingly the open-circuit potential also increases by 55 mV, clearly revealing the formation of many of these groups, which usually happens because of the creation of functional groups due to oxidation. Oxidative unzipping, which increases the surface area per SWNT, also enhances the capacitance, accounting for the increase in area as well as the formation of functional groups (especially, oxygen-containing functional groups). After selective reduction of SWNT oxide at −0.7 V for 7 h, there is a gradual decrease in the capacitance ascribed to the removal of oxygen functionalities (from X-ray photoelectron spectra in ref 18) from unzipped tubes implying faster kinetics compared to that during the oxidation step.[33] Peaks at −0.57 and −0.38 V correspond to oxygen reduction and hydroxide formation.

In addition to the electric field effects as addressed above, structural characteristics of SWNTs such as chirality and diameter could also lead to specified preferences for the unzipping process, as evidenced by the *in situ* Raman spectroscopic measurements. In order to clarify their influence and to understand further the fundamental role of oxygen in unzipping, we have performed calculations using the spin-polarized density-functional tight-binding (DFTB) method. On the basis of geometrical optimization of three sets of SWNTs with different chiralites and diameters, relative energy changes in forming epoxy groups on the outer walls were studied. We classify carbon nanotubes by their diameter into three sets; the first set includes chiralities (4, 4), (5, 2), and (7, 0), the second set (5, 5), (6, 3), and (9, 0), and the last set (6, 6), (7, 4), and (11, 0). All three sets of SWNTs have lengths between 2 and 3 nm. Both ends of the SWNTs are terminated chemically by hydrogen atoms.

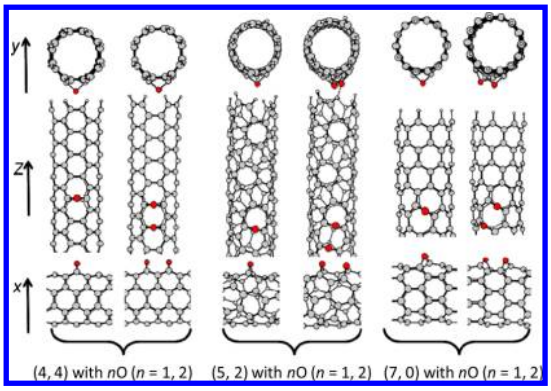

Figure 6. Optimized configurations of (4, 4), (5, 2), and (7, 0) SWNTs with *n*O (*n* = 1, 2) by self-consistent charge formalism (SCC-DFTB-D). These chiralities were chosen so that the *n*O addition is visually identifiable along with clarity in the direction of oxygen addition. A number of various chiralitites were used for the DFTB-D study of the dependence of the *n*O binding energy on the oxygen attachment direction and diameter of the SWNT.

By forming epoxy groups on graphitic carbon structures, the underlying sp^2 carbon–carbon bonds will be elongated; thus SWNTs can be unzipped, or cut, by oxidation into graphene nanoribbons with specific width depending on the structures of SWNTs.[34] It is shown that, by preferential aligning, the total energy of epoxidized SWNTs could be lowered.[35,36] As illustrated in Figure S14, there are several possible pathways for cutting by binding oxygen atoms, as described by their relative orientation to the axis of SWNTs. In the first set of SWNTs for example, there are two cutting directions for armchair (4, 4) nanotubes, with different angles to the axis, 0° and 30°, respectively. For chiral (5, 2) SWNTs, angles are 16.1°, 52.9°, and 76.1°, and for zigzag (7,0) SWNTs, the angles are 30° and 60° for zigzag nanotube (7,0). The other two sets have similar cutting mechanisms with multiple pathways. All the structures have been optimized, and the most stable structures in the first set of SWNTs and their oxidized derivatives are shown in Figure 6. For the armchair and chiral SWNTs, the ground states of the products are closed-shell singlet, while for zigzag ones, quintet states with four unpaired electrons on the nanotube ends are preferred energetically. The energies of epoxidized structures with one and two oxygen atoms are listed in Table S2.

According to the Bell–Evans–Polanyi (BEP) principle, the difference in activation energy between two reactions of the same family is proportional to the

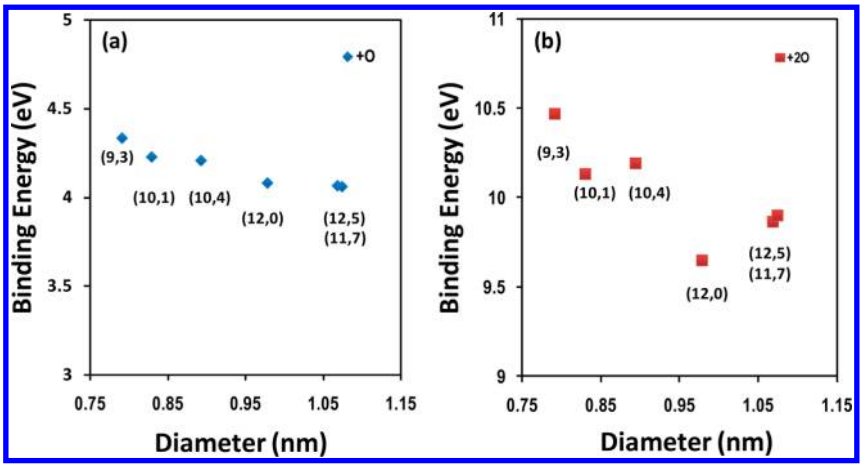

Figure 7. Dependance of oxygen binding on the diameter of SWNT. Variation of the binding energy (E_b) of the SWNTs + O (n = 1, blue data) (a) and (n = 2, maroon) (b) with the diameter of SWNTs.

difference of their enthalpy of reactions. Thus the binding energies calculated here offer explicit evidence to assess the reaction barrier of SWNT oxidation.[37] This is confirmed by direct comparison between calculated binding energies and reaction barriers using the climbing nudged energy band (CNEB) method using the first-principles method (details given in the Supporting Information as text and Figure S15). From the results we can clearly see that, for SWNTs with the same chirality, it turns out that SWNTs with smaller diameters have higher oxygen-binding energies; that is, one oxygen cutting through epoxidation is energetically more favorable for SWNTs with smaller diameters than those with larger diameters. As an example, E_b for (7, 0) is 5.1436 eV, while for (9, 0) and (11, 0), it is 4.3011 and 4.1384 eV, respectively. For all structures under investigation, we find the direction of epoxidation prefers to be aligned to the nanotube axis. There is also a distinct dependence of E_b on the angle of chirality θ (for a nanotube with chiral index (n, m), $\theta = \tan^{-1}[\sqrt{3}m/(m + 2n)]$, *e.g.*, $\theta = 0°$ and 30° for zigzag and armchair CNTs, respectively) of an SWNT, as shown in Figure S16. As the chiral angle of graphene lattice increases, E_b decreases and the binding of oxygen atoms through epoxy groups is less preferred.

In order to correlate the DFT calculations with the *in situ* Raman spectroscopic observations, we have performed similar calculations for SWNTs with the chiralities, the same as in the Raman studies (Table S3 and Figure S17). The calculations matched well with our experimental results for certain SWNTs, as the binding energies of 2O addition for (12, 0), (12, 5), and (11, 7) with relatively large diameters are 9.65, 9.86, and 9.90 eV, whereas for (9, 3), (10, 1), and (10, 4) the binding energies are 10.47, 10.14, and 10.20 eV, respectively (Figure 7). The data indicate that, for the first three SWNTs, oxygen addition is more difficult when compared to the later ones. The energetics of oxygen addition is a direct measure of the ease of unzipping; that is, (9, 3) and (10, 1) can be be unzipped with lesser energy (low electrode potentials), whereas (12, 5) and (11, 7) need relatively higher energy to get unzipped. These structural characteristics, with additional effects of the applied field clarified above (not included in the calculations), and potentially the interaction between substrate and SWNTs[38] determine the preference of oxidation and cutting processes of SWNTs.

CONCLUSIONS

Here we report an *in situ* Raman spectroscopic and microscopic investigation of the electrochemical unzipping of SWNTs. From careful observation of the RBMs and by using inputs from resonant Raman scattering theory, we understand that two types of metallic SWNTs with chiralities (10, 4) and (12, 0) are opened up rapidly at 0.36 V followed by a gradual opening of another two metallic SWNTs with chiralities (9, 3) and (10, 1) at 1.16 V. This is again followed by the slow unzipping of another two kinds of semiconducting nanotubes with chiralities (11, 7) and (12, 5) at a relatively high potential (−1.66 V). It has been observed that smaller size SWNTs are unzipped at relatively low electrode potentials. A gradual decrease in the metallicity of the SWNT ensemble was confirmed from the careful observation of the width of the G band. An increase in the D (defect) band with retention of the 2D band suggests unzipping of nanotubes forming graphene ribbons. A CV study confirms selective oxidation of SWNTs at an applied potential of 0.7 V for 7 h. Oxidative unzipping is evidenced by the improvement in capacitance. In the next reduction step, SWNT-oxide becomes graphene, which is clear from the subtle changes in the voltammograms with a decrease in the capacitance. On the basis of DFTB calculations, we show that there is a dependence of the diameter and chirality of an SWNT on the binding energies of single and double oxygen atoms as in-line epoxy groups. This trend is similar to the *in situ* Raman spectroscopic

observations, suggesting that the mechanism of unzipping is likely to be the formation of epoxides on SWNTs and their successive transformation to graphene ribbons.

METHODS AND MATERIALS

Preparation of the SWNT Sample. The sample of SWNTs from Carbon Nanotechnologies Inc., which is a mixture of semiconducting and metallic nanotubes, was purified according to the following protocol. The mixture was heated for 12 h at 250 °C in a furnace. It was further treated with 15 mL of concentrated HCl, thereby removing the metal catalysts as their chlorides. The acid-treated sample was then filtered using a membrane (0.2 μm pore size) filter to obtain bucky paper, which was neutralized with a 1 M solution of $NaHCO_3$, until the filtrate showed a pH greater than 7.0. The unreacted acid was removed followed by washing with copious amounts of water. The residue collected was dried at 70 °C for 6 h and preserved under vacuum until further use. The dispersion of the purified SWNT was prepared by taking 1 mg of the sample in 10 mL of dimethyl formamide (purchased from Qualigens) and sonicating it for 2 h with control over temperature.

Electrochemical Cell for *in Situ* Raman Measurements. A 50 μL sample of the SWNT dispersion in DMF was drop casted on the working electrode of the electrochemical cell. The cell was designed in such a way that both the electrodes (working and counter) are on the conducting side of the indium-doped tin oxide coating (conductivity of 40 Ω cm^{-1}, purchased from Nikon Sheet Glass Ltd.). We made a discontinuity on the conducting side of the glass slide by removing the conducting layer by scratching to create the electrodes (inset of Figure 1). The cell was covered with a coverglass, through which the process of unzipping can be observed using Raman spectroscopy. Three sides of the cell were sealed with Teflon tape to make it a cavity with one side open in order to allow the insertion of the electrolyte. The electrolyte (0.5 M H_2SO_4) was injected into the cell with the help of a syringe, which was then distributed into the cell by means of capillary action as a cell column thickness of around 0.15 mm was used. A coverglass-corrected (∞/0.17) 100$\times$ oil immersion objective (NA 1.3) whose working distance is 0.23 mm was used for spectral measurements. The potential was applied using a dc source in the range -5.0 to $+5.0$ V.

Confocal Raman Spectroscopy and Imaging. Confocal Raman measurements were done with a WiTec GmbH, CRM αS300 instrument having a 532 nm Nd:YAG laser as the excitation source. The effective scan range of the spectrometer was 0$-$3800 cm^{-1} with a 600 grooves/mm grating, and the dispersed light intensity was measured by a Peltier-cooled charge coupled device (CCD). Raman imaging was done using the same grating, with an integration time of 100 ms. The piezoelectric scanner with maximum scanning area of 100 μm $\times$ 100 μm enabled the movement of the electrochemical cell (which is at the focal plane of the objective) for scanning. Each image contains 200 pixels in 200 lines (40 000 pixels) with each pixel having a Raman spectrum of a particular spatial position. Single-spot spectra were also acquired with larger integration times. For improved resolution and to ascertain peak positions, 1800 grooves/mm grating was used while acquiring single-spot spectra. The intensities of the desired portion of the spectra, collected over all of the pixels, were compared by Scan CTRL Spectroscopy Plus Version 1.32 software, to construct color-coded images. Also, the image corresponding to various features of graphene, namely, RBM I, RBM II, RBM III, D, G, and 2D, was filtered from the image using WiTec Project 3.2.

Transmission Electron Microscopy. TEM imaging was performed using a JEOL 3010 instrument. The accelerating potential used for imaging the graphene ribbons was 200 kV. The sample was drop cast on a copper grid and was dried in ambient conditions prior to the TEM analysis.

Density Functional Theory Calculations. All calculations here are carried out using the DFTB+ program.[39,40] DFTB is an approximate density functional theory method based on the tight-binding approach that utilizes an optimized minimal linear combination of atomic orbital (LCAO) Slater-type all-valence basis set and a two-center approximation for Hamiltonian matrix elements. The Coulombic interaction between partial atomic charges was determined using the self-consistent charge (SCC) formalism. Slater$-$Kirkwood-type dispersion was employed for van der Waals and $\pi-\pi$ stacking interactions. This approach has been shown to give a reasonably good prediction of carbon nanostructures and their functional derivatives.[41,42]

Conflict of Interest: The authors declare no competing financial interest.

Acknowledgment. T.P. thanks DST for financial support through the Nano Mission. R.J. thanks UGC for a fellowship. Mr. C. R. Arunkumar, CSM, POSTECH, South Korea, is thanked for initial discussions on DFT. Prof. Shigeo Maruyamma and Mr. Pei Zhao are thanked for technical advice on indexing the chiralities of SWNTs. Mr. Anirban Som is thanked for TEM measurements. V.K.P. and D.B.S. acknowledge financial support of CSIR through the project NWP0022.

Supporting Information Available: Raman images filtered from RBM I, RBM II, RBM III, D band, G band, and 2D band for all eight electrochemical conditions (steps) are given along with the average Raman spectra obtained from automated cluster analysis (which showed similarity to the manually averaged spectra) by the WiTec Project software. TEM images are also included to show the unzipped SWNTs. Supporting evidence for the Bell$-$Evans$-$Polanyi principle by additional first-principles calculations is provided, which compares binding energies of oxygen atoms and the reaction barriers. This material is available free of charge *via* the Internet at http://pubs.acs.org.

REFERENCES AND NOTES

1. Kroto, H. W.; Heath, J. R.; O'Brien, S. C.; Curl, R. F.; Smalley, R. E. C60: Buckminsterfullerene. *Nature* **1985**, *318*, 162–168.
2. Iijima, S. Helical Microtubules of Graphitic Carbon. *Nature* **1991**, *354*, 56–58.
3. Novoselov, K. S.; Geim, A. K.; Morozov, S. V.; Jiang, D.; Zhang, Y.; Dubonos, S. V.; Grigorieva, I. V.; Firsov, A. A. Electric Field Effect in Atomically Thin Carbon Films. *Science* **2004**, *306*, 666–669.
4. Lin, Y. M.; Dimitrakopoulos, C.; Jenkins, K. A.; Farmer, D. B.; Chiu, H. Y.; Grill, A.; Avouris, Ph. 100-GHz Transistors from Wafer-Scale Epitaxial Graphene. *Science* **2010**, *327*, 662.
5. Kedzierski, J.; Hsu, P. L.; Healey, P.; Wyatt, P. W.; Keast, C. L.; Sprinkle, M.; Berger, C.; de Heer, W. A. Epitaxial Graphene Transistors on SiC Substrates. *IEEE Trans. Electron Devices* **2008**, *55*, 2078–2085.
6. Schwierzl, F. Graphene Transistors. *Nat. Nanotechnol.* **2010**, *89*, 487–496.
7. Candini, A.; Klyatskaya, S.; Ruben, M.; Wernsdorfer, W.; Affronte, M. Graphene Spintronic Devices with Molecular Nanomagnets. *Nano Lett.* **2011**, *11*, 2634–2639.
8. Shiomi, J.; Maruyama, S. Diffusive-Ballistic Heat Conduction of Carbon Nanotubes and Nanographene Ribbons. *Int. J. Thermophys.* **2010**, *31*, 1945–1951.
9. Brar, V. W.; Wickenburg, S.; Panlasigui, M.; Park, C. H.; Wehling, T. O.; Zhang, Y.; Decker, R.; Girit, C.; Balatsky, A. V.; Louie, S. G.; *et al*. Observation of Carrier-Density-Dependent Many-Body Effects in Graphene *via* Tunneling Spectroscopy. *Phys. Rev. Lett.* **2010**, *104*, 036805 (1$-$4).
10. Novoselov, K. S.; Jiang, Z.; Zhang, Y.; Morozov, S. V.; Stormer, H. L.; Zeitler, U.; Maan, J. C.; Boebinger, G. S.; Kim, P.; Geim, A. K. Room-Temperature Quantum Hall Effect in Graphene. *Science* **2007**, *315*, 1379.

11. Levy, N.; Burke, S. A.; Meaker, K. L.; Panlasigui, M.; Zettl, A.; Guinea, F.; Castro Neto, A. H; Crommie, M. F. Strain-Induced Pseudo Magnetic Fields Greater Than 300 T in Graphene Nanobubbles. *Science* **2010**, *329*, 544–547.
12. Shinde, D. B.; Pillai, V. K. Electrochemical Resolution of Multiple Redox Events for Graphene Quantum Dots. *Angew. Chem., Int. Ed.* **2013**, *52*, 2482–2485.
13. Wallace, P. R. The Band Theory of Graphite. *Phys. Rev.* **1947**, *71*, 622–634.
14. Odom, T. W.; Huang, J. L.; Kim, P.; Lieber, C. M. Atomic Structure and Electronic Properties of Single-Walled Carbon Nanotubes. *Nature* **1998**, *391*, 62–64.
15. Nakada, K.; Fujita, M.; Dresselhaus, G.; Dresselhaus, M. S. Edge State in Graphene Ribbons: Nanometer Size Effect and Edge Shape Dependence. *Phys. Rev. B* **1996**, *54*, 17954–17961.
16. Han, M. Y.; Ozyilmas, B.; Zhang, Y.; Kim, P. Energy Band-Gap Engineering of Graphene Nanoribbons. *Phys. Rev. Lett.* **2007**, *98*, 206805(1−4).
17. Son, Y. W.; Cohen, M. L.; Louie, S. G. Energy Gaps in Graphene Nanoribbons. *Phys. Rev. Lett.* **2006**, *97*, 216803 (1−4).
18. Mohanty, N.; Moore, D.; Xu, Z.; Sreeprasad, T. S.; Nagaraja, A.; Rodriguez, A. A.; Berry, V. Nanotomy-Based Production of Transferable and Dispersible Graphene Nanostructures of Controlled Shape and Size. *Nat. Commun.* **2012**, *3*, 844(1−8).
19. Huang, L. F.; Zhang, G. R.; Zheng, X. H.; Gong, P. L.; Cao, T. F.; Zeng, Z. Understanding and Tuning the Quantum-Confinement Effect and Edge Magnetism in Zigzag Graphene Nanoribbon. *J. Phys.: Condens. Matter.* **2013**, *25*, 055304 (1−8).
20. Chen, Z.; Lin, Y. M.; Rooks, M. J.; Avouris, Ph. Graphene Nanoribbon Electronics. *Phys. E (Amsterdam, Neth.)* **2007**, *40*, 228–232.
21. Wang, X.; Ouyang, Y.; Li, X.; Wang, H.; Guo, J.; Dai, H. Room-Temperature All-Semiconducting Sub-10-nm Graphene Nanoribbon Field-Effect Transistors. *Phys. Rev. Lett.* **2008**, *100*, 206803(1−4).
22. Maeda, Y.; Kimura, S.; Kanda, M.; Hirashima, Y.; Hasegawa, T.; Wakahara, T.; Lian, Y.; Nakahodo, T.; Tsuchiya, T.; Akasaka; *et al*. Large-Scale Separation of Metallic and Semiconducting Single-Walled Carbon Nanotubes. *J. Am. Chem. Soc.* **2005**, *127*, 10287–10290.
23. Heller, D. A.; Mayrhofer, R. M.; Baik, S.; Grinkova, Y. V.; Usrey, M. L.; Strano, M. S. Concomitant Length and Diameter Separation of Single-Walled Carbon Nanotubes. *J. Am. Chem. Soc.* **2004**, *126*, 14567–14573.
24. Shinde, D. B.; Debgupta, J.; Kushwaha, A.; Aslam, M.; Pillai, V. K. Electrochemical Unzipping of Multi-walled Carbon Nanotubes for Facile Synthesis of High-Quality Graphene Nanoribbons. *J. Am. Chem. Soc.* **2011**, *133*, 4168–4171.
25. Kosynkin, D. V.; Higginbotham, A. L.; Sinitskii, A.; Lomeda, J. R.; Dimiev, A.; Price, B. K.; Tour, J. M. Longitudinal Unzipping of Carbon Nanotubes to Form Graphene Nanoribbons. *Nature* **2009**, *458*, 872–876.
26. Elias, A. L.; Botello-Mendez, A. R.; Meneses-Rodriguez, D.; Gonzalez, V. J.; Ramirez-Gonzalez, D.; Ci, L.; Munoz-Sandoval, E.; Ajayan, P. M.; Terrones, H.; Terrones, M. Longitudinal Cutting of Pure and Doped Carbon Nanotubes to Form Graphitic Nanoribbons Using Metal Clusters as Nanoscalpels. *Nano Lett.* **2010**, *10*, 366–372.
27. Jorio, A.; Saito, R.; Hafner, J. H.; Lieber, C. M.; Hunter, M.; McClure, T.; Dresselhaus, G.; Dresselhaus, M. S. Structural (*n*,*m*) Determination of Isolated Single-Wall Carbon Nanotubes by Resonant Raman Scattering. *Phys. Rev. Lett.* **2007**, *86*, 1118–1121.
28. Dresselhaus, M. S.; Dresselhaus, G.; Saito, R.; Jorio, A. Exciton Photophysics of Carbon Nanotubes. *Annu. Rev. Phys. Chem.* **2007**, *58*, 719–747.
29. Araujo, P. T.; Doorn, S. K.; Kilina, S.; Tretiak, S.; Einarsson, E.; Maruyama, S.; Chacham, H.; Pimenta, M. A.; Jorio, A. Third and Fourth Optical Transitions in Semiconducting Carbon Nanotubes. *Phys. Rev. Lett.* **2007**, *98*, 067401(1−4).
30. Dresselhaus, M. S.; Jorio, A.; Souza Filha, A. G.; Dresselhaus, G.; Saito, R. Raman Spectroscopy on One Isolated Carbon Nanotubes. *Phys. B (Amsterdam, Neth.)* **2002**, *323*, 15–20.
31. dos Santos, R. P. B.; Perim, E.; Autreto, P. A. S.; Brunetto, G.; Galvao, D. S. On the Unzipping of Multiwalled Carbon Nanotubes. *Nanotechnology* **2012**, *23*, 465702(1−7).
32. Kim, W. S.; Moon, S. Y.; Bang, S. Y.; Choi, B. G.; Ham, H.; Sekino, T.; Shim, K. B. Fabrication of Graphene Layers from Multiwalled Carbon Nanotubes Using High DC Pulse. *Appl. Phys. Lett.* **2009**, *95*, 0831031–0831033.
33. Ramesha, G. K.; Sampath, S. Electrochemical Reduction of Oriented Graphene Oxide Films: An *in-Situ* Raman Spectroelectrochemical Study. *J. Phys.Chem. C* **2009**, *113*, 7985–7989.
34. Jiang, L.; Zhang, L.; Wang, X.; Diankov, G.; Dai, H. Narrow Graphene Nanoribbons from Carbon Nanotubes. *Nature* **2009**, *458*, 877–880.
35. Li, J. L.; Kudin, K. N.; McAllister, M. J.; Prud'homme, R. K.; Aksay, I. A.; Car, R. Oxygen-Driven Unzipping of Graphitic Materials. *Phys. Rev. Lett.* **2006**, *96*, 176101(1−4).
36. Xu, Z.; Xue, K. Engineering Graphene by Oxidation: A First-Principles Study. *Nanotechnology* **2010**, *21*, 045704–045707.
37. Aradi, B.; Hourahine, B.; Frauenheim, T. DFTB+, a Sparse Matrix-Based Implementation of the DFTB Method. *J. Phys. Chem. A* **2007**, *111*, 5678–5684.
38. Evans, M. G.; Polanyi, M. Inertia and Driving Force of Chemical Reactions. *Trans. Faraday Soc.* **1938**, *34*, 11–24.
39. Zhang, C.; Bets, K.; Lee, S. S.; Sun, Z.; Mirri, F.; Colvin, V. L.; Yakobson, B. I.; Tour, J. M.; Hauge, R. H. Closed-Edged Graphene Nanoribbons from Large-Diameter Collapsed Nanotubes. *ACS Nano* **2012**, *6*, 6023–6032.
40. DFTB code can be found at http://www.dftb.org.
41. Zheng, G.; Elstner, S. M.; Morokuma, K. Performance of the DFTB Method in Comparison to DFT and Semiempirical Methods for Geometries and Energies of C20−C86 Fullerene Isomers. *Chem. Phys. Lett.* **2005**, *412*, 210–216.
42. Gao, X. F.; Liu, L. L.; Irle, S.; Nagase, S. Carbon Spiral Helix: A Nanoarchitecture Derived from Monovacancy Defects in Graphene. *Angew. Chem., Int. Ed.* **2010**, *49*, 3200–3202.